

# Coherent Electron Transport across a 3 nm Bioelectronic Junction Made of Multi-Heme Proteins

Zdenek Futera, Ichiro Ide, Ben Kayser, Kavita Garg, Xiuyun Jiang, Jessica H. van Wonderen, Julea N. Butt, Hisao Ishii, Israel Pecht, Mordechai Sheves, David Cahen, and Jochen Blumberger\*



Cite This: *J. Phys. Chem. Lett.* 2020, 11, 9766–9774



Read Online

ACCESS |



Metrics & More

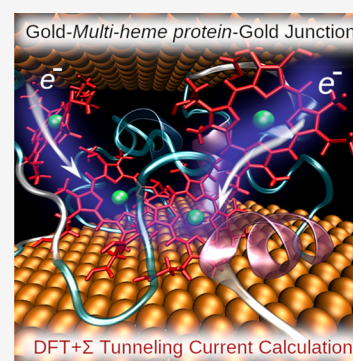


Article Recommendations



Supporting Information

**ABSTRACT:** Multi-heme cytochromes (MHCs) are fascinating proteins used by bacterial organisms to shuttle electrons within, between, and out of their cells. When placed in solid-state electronic junctions, MHCs support temperature-independent currents over several nanometers that are 3 orders of magnitude higher compared to other redox proteins of similar size. To gain molecular-level insight into their astonishingly high conductivities, we combine experimental photoemission spectroscopy with DFT+ $\Sigma$  current–voltage calculations on a representative Gold-MHC-Gold junction. We find that conduction across the dry, 3 nm long protein occurs via off-resonant coherent tunneling, mediated by a large number of protein valence-band orbitals that are strongly delocalized over heme and protein residues. This picture is profoundly different from the electron hopping mechanism induced electrochemically or photochemically under aqueous conditions. Our results imply that the current output in solid-state junctions can be even further increased in resonance, for example, by applying a gate voltage, thus allowing a quantum jump for next-generation bionanoelectronic devices.



Redox-active metalloproteins are ubiquitous in living organisms facilitating many of the energy conversion processes that are quintessential for life on earth including photosynthesis, respiration, and nitrogen fixation. Recently, multi-heme cytochromes (MHC) and their complexes have gained much attention due to their involvement in extracellular respiration and interspecies electron exchange in dissimilatory metal-reducing bacteria.<sup>1–3</sup> Atomic X-ray structures of several of these proteins were resolved for *S. oneidensis*,<sup>4–8</sup> and very recently also for *G. sulfurreducens*,<sup>9,10</sup> revealing closely packed heme *c* cofactor arrangements within the protein peptide matrices suggestive of their function as “biological nanowires”. MHC protein complexes<sup>8</sup> or polymers<sup>9,10</sup> span the entire bacterial envelope, thereby facilitating the export of electrons from the inside to the outside of the cell. Experiments,<sup>11,12</sup> theory,<sup>13</sup> and computation<sup>14–17</sup> have given valuable insights into the thermodynamics, kinetics, and the mechanistic aspects of this process, in particular suggesting that electron transfer (ET) across these structures in their native (aqueous) environments occurs by consecutive heme-to-heme electron hopping.<sup>14–16,18</sup>

For nanotechnological applications, interfaces of the metalloproteins with solid electrodes are of great interest, and their properties are intensively studied because of their potential utilization in enzymatic biofuel production, bioelectrocatalysis, biosensors, and molecular (bio)electronics.<sup>19–21</sup> Recently, we demonstrated that MHCs are significantly better electronic conductors than other proteins in junctions composed of solid protein monolayers in contact with two gold electrodes.<sup>22</sup> Most strikingly, the small tetra-heme cytochrome (STC) was

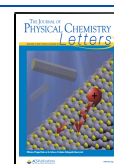
found to have a conductance 3 orders of magnitude higher than that of the blue copper protein azurin,<sup>23</sup> even though both proteins have similar cross sections. Exceptionally large current densities (normalized to length) were also obtained for the deca-heme protein MtrF,<sup>22</sup> which were comparable with the STM single molecule currents reported earlier for MtrF,<sup>24</sup> MtrC,<sup>25</sup> and OmcA<sup>25</sup> (see analysis in ref 14).

Unfortunately, we currently still lack a good understanding of the atomistic origin of the large conductivities observed for solid-state MHC junctions, in contrast to our knowledge of their ET properties in aqueous solution.<sup>3</sup> This is highly unsatisfactory as it prevents us from rationally engineering multi-heme proteins for next-generation bionanoelectronic devices. While early single molecule STM measurements of MHCs were interpreted in terms of inelastic and elastic tunneling models,<sup>1,26</sup> more recent STM tunneling currents were modeled by assuming activated heme-to-heme hopping similarly as for ET in solution.<sup>24,27</sup> Nevertheless, the latest measurements by Garg et al. on MHC monolayer junctions showed virtually zero temperature dependence between 320 and 80 K, pointing to tunneling as the dominant conduction mechanism over this temperature range.<sup>22</sup> This is an

Received: September 2, 2020

Accepted: October 20, 2020

Published: November 3, 2020



unexpected and highly significant result because it exceeds the traditional “coherent tunneling limit” for biological electron transfer ( $\sim 1.5$  nm) by a factor of 2. Here we combine electronic structure calculations with ultraviolet photoemission spectroscopy to gain molecular-level insight into the conduction process.

Ideally, one would compute the electronic states and current–voltage characteristic from first-principles, but so far this has been considered intractable for systems as large as entire proteins, let alone proteins between two metal electrodes. Building on recent methodological advances,<sup>28</sup> we demonstrate that such calculations are now possible. We report the calculation of the current–voltage response of a multi-heme protein junction where the electronic structure of the full protein and both gold electrodes are treated at the DFT+ $\Sigma$  level of theory ( $\approx 20000$  electrons). To the best of our knowledge, this is the first time that conductance calculations of this kind are reported for systems as large as entire redox protein in junctions. The calculations are performed on adsorption structure determined by molecular dynamics (MD) simulations and supported by ultraviolet photoemission spectroscopy (UPS) measurements which are used to determine the energy level alignment of protein states with respect to the Fermi level of the electrodes. We find strong evidence that electronic conduction is in the off-resonant coherent tunneling regime, mediated by a manifold of valence band orbitals that are delocalized over heme and protein amino acids and effectively “gating” the current between the two electrodes.

Experimental current–voltage ( $I$ – $V$ ) and current–temperature ( $I$ – $T$ ) curves are available for the tetra-heme protein STC with Cys introduced at site 87 which allows for chemisorption on the bottom gold electrode surface.<sup>22</sup> We first analyze the available experimental data by fitting the measured curves to incoherent and coherent transport models (Figure 1a) to show the qualitative differences between these two limiting charge transport mechanisms. It is well-known that in aqueous solution the ET through STC occurs via incoherent heme-to-heme hopping. Hence, we investigate the same mechanism for the modeling of electronic conduction. The steady-state current at a given voltage was obtained by solving a chemical master equation assuming nearest-neighbor hopping.<sup>13,15,16</sup> The heme–heme hopping rate constants and the interfacial ET rates from/to the electrodes are calculated by using the nonadiabatic Marcus expressions<sup>29,30</sup> where the voltage is assumed to modify only the heme-cofactor redox potentials. Two possible adsorption geometries of the protein were investigated: a “standing” structure where the four-heme chain connects the two electrodes (Figure 1b), as suggested in our earlier work,<sup>22</sup> and a “lying” structure, motivated by the adsorption geometry discussed below in this work, with two potential hopping pathways (see Figure 1c). Further details on the incoherent hopping model and the fitting parameters are given in the Supporting Information. Although it is possible to fit the  $I$ – $V$  and  $I$ – $T$  curves separately with two different sets of fit parameters, we find that neither of the two hopping models can capture both curves with a single set of fit parameters (Figure 1a). A good fit of the  $I$ – $V$  curve (indicated in yellow and red in Figure 1a for the two models) gives a too strong temperature dependence (inset), whereas a good fit of the  $I$ – $T$  curve requires very small reorganization free energies of  $<0.1$  eV and gives a qualitatively wrong shape of the  $I$ – $V$  curve.

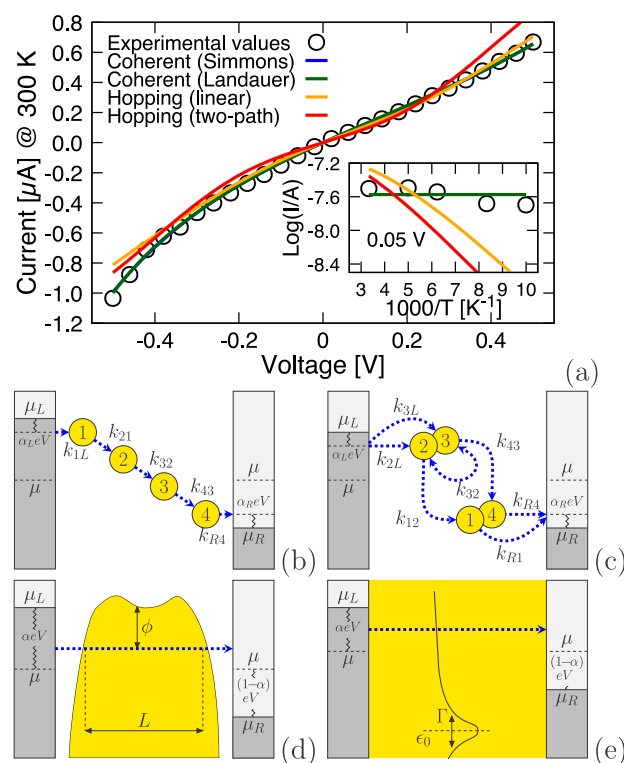


**Figure 1.** (a) Current–voltage ( $I$ – $V$ ) and current–temperature ( $I$ – $T$ ) curves (inset) for the tetra-heme protein STC. The experimental data are obtained for a protein monolayer in a vacuum by using the suspended nanowire technique.<sup>22</sup> Best fits of the experimental data are shown for incoherent hopping models (b) along a linear chain and (c) along a branched chain of heme cofactors as well as for coherent tunneling models according to Simmons (d) and Landauer (e). Note that the coherent models of Simmons and Landauer predict the same fit, and their curves are on top of each other.  $\mu_L$  and  $\mu_R$  are the Fermi levels of the left (L) and right (R) electrode, and  $\alpha$  is the symmetry factor of the potential drop. In (b) and (c)  $k_{ij}$  indicate the rate constant for ET from site  $i$  to site  $j$ , and 1–4 denote the four heme cofactors. In (d)  $L$  denotes the tunneling length and  $\phi$  the tunneling barrier, and in (e)  $\Gamma$  and  $\epsilon_0$  are the width and position, respectively, of the effective conduction channel. See the Supporting Information for details.

In contrast to incoherent models, fully coherent electron tunneling does not *a priori* exhibit any temperature dependence (apart from that of the Fermi–Dirac distribution function), and therefore this mechanism seems to be more appropriate to explain the measured data in the STC junction. Here, we modeled the  $I$ – $V$  curves by the popular Simmons model,<sup>31</sup> assuming electron tunneling between the two electrodes through a single potential barrier, and by the Landauer model with one effective conduction channel.<sup>32–34</sup> Both models reproduce the  $I$ – $V$  curves very well ( $R^2 > 0.99$ ; see the Supporting Information for model details and values of the fitting parameters). Therefore, we conclude that the conduction is well described by standard coherent tunneling models. To obtain a deeper, molecular-level insight into the conduction process, we will identify in the following the molecular orbital(s) of the STC protein and the structural features (Fe, heme, and amino acids) that contribute to the current via explicit electronic structure calculations on the full Gold-STC-Gold junction. This requires an atomistic structural model of the junction.

Because  $I$ – $V$  measurements<sup>22</sup> were performed in a vacuum ( $10^{-5}$  bar), we first verified using molecular dynamics (MD) simulation that the STC protein remains folded and stable under these conditions. Indeed, the RMSD remained rather small, 1.5 Å with respect to the crystal structure, along a trajectory of length 40 ns. The robust secondary structure is a result of strong covalent binding of the rigid heme cofactors to the protein matrix via cysteine linkages and of axial coordination of the heme iron cations to two proximal histidines.

The adsorption of the S87C mutant on the Au(111) surface, which is the predominant orientation of the polycrystalline Au thin films, was simulated by the GoIP-CHARMM force field,<sup>35,36</sup> capturing the image charge effects and providing thus fairly good adsorption structures and energies.<sup>37</sup> The adsorption structures generated could be clustered in two groups: the “standing” configuration where the heme chain is orthogonal to the gold surface and the “lying” configuration where the heme chain is parallel to the surface (Figure 2a). From these, only the lying structures are within the experimental range 2.4 ± 0.5 nm of monolayer thickness<sup>22</sup> (blue area in Figure 2a). Therefore, we chose the horizontal structure with the smallest RMSD (2.3 Å compared to STC crystal structure; indicated by an arrow in Figure 2a), which also turned out to have one of the highest adsorption energies.

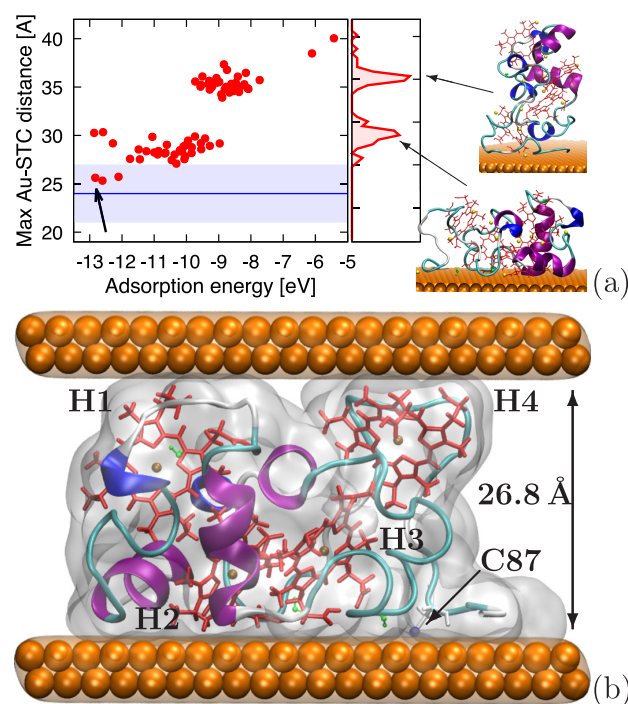


**Figure 2.** Adsorption structures of STC on Au(111) as obtained from docking and MD simulation. In (a) the largest distance of any protein atom in the surface-normal direction is plotted against adsorption energy for generated samples. The structures can be clustered in two distinct adsorption geometries: “lying” and “standing” (red distributions with representative structures indicated). The experimental range and mean value of monolayer thickness are indicated in (a) by the shaded area and the blue line, respectively. In (b) the “lying” structure indicated by an arrow in (a) is shown after the top electrode contact is added. The protein is chemisorbed to the bottom electrode contact via Cys-87 and physisorbed to the top electrode. The heme cofactors are shown in red and secondary structure elements of STC in cartoon representation.

This structure was chemisorbed to the surface by specifying a covalent interaction between the sulfur atom of Cys-87 and gold using the Au–S covalent interaction parameters fitted previously to DFT calculations at the van der Waals density functional level.<sup>37</sup> To complete the structural model of the junction, the top electrode contact was placed at close contact with the upper protein surface. After protein relaxation, the distance between the two electrodes was varied until the local pressure tensor in the protein region integrated to zero.<sup>38</sup> The final electrode separation obtained was 2.7 nm, in good agreement with experimental measurements,  $2.4 \pm 0.5$  nm.<sup>22</sup> In the final protein structure (shown in Figure 2b) hemes 2 and 3 are in proximity with the bottom contact, whereas hemes 1 and 4 are close to the upper contact, thus forming a bifurcated heme path between the electrodes. This structure was used for electronic structure and  $I$ – $V$  calculations at the DFT+ $\Sigma$  level, as detailed below.

The electronic structure calculations on the full Gold-STC-Gold model junction were performed with the CP2K software package using the PBE functional, GTH pseudopotentials, and the DZVP basis set.<sup>39–41</sup> The electronic states obtained from KS calculations were localized on protein and gold electrodes and diagonalized within the respective subspaces by using the projector operator-based diabatization method (POD).<sup>28</sup> Although the PBE functional can describe metallic states of gold rather well, it suffers from an inaccurate band alignment of the protein energy levels,  $\epsilon_{p,j}$ , with respect to the Fermi level of the electrode,  $E_F$ . Here we use the DFT+ $\Sigma$  method<sup>42–44</sup> to correct for this deficiency (see the Supporting Information, section S5.3 and eqs S38–S39). This results in a shift of the occupied protein energy levels by 1.2 eV downward,  $\epsilon_{\Sigma,j}$  (occupied) =  $\epsilon_{p,j}$  (occupied) – 1.2 eV, placing the protein HOMO at –1.2 eV with respect to the Fermi level. The unoccupied protein levels are shifted upward by 1.4 eV,  $\epsilon_{\Sigma,j}$  (unoccupied) =  $\epsilon_{p,j}$  (unoccupied) + 1.4 eV, placing the protein LUMO at +1.4 eV with respect to the Fermi level. Although one cannot expect DFT+ $\Sigma$  to be quantitative in general,<sup>45</sup> the predicted HOMO alignment is for the present system in very good agreement with ultraviolet photoelectron spectroscopy (UPS) and constant final state (CFS) yield spectroscopy measurements performed on the STC/gold interface (see Figure 3 for experimental details).

The electronic structure of the Gold-STC-Gold junction as obtained from DFT+ $\Sigma$  calculations is shown in Figure 3c. The total projected density of states is broken down in contributions from Fe atoms (denoted “Iron”), the porphyrin rings and axial histidines ligating Fe (collectively denoted “Heme”), all amino acid residues except the axial histidines (denoted “Protein”), and gold. We find that the highest valence band states of the protein give rise to three distinct peaks between –1.2 and –1.8 eV and correspond to Fe  $d$   $t_{2g}$  states hybridized with orbitals from the porphyrin ring, the axial histidines, and partly also on the cysteine linkages of the heme cofactors. Some of these states are localized on a single heme while others are delocalized over up to all four heme groups of STC. The iron band is mixed with the highest protein amino acid electronic states localized on Met-67 (–1.3 eV) in the middle of the junction, Asp-81 (–1.4 eV) near the upper gold surface, and N-terminal acetyl (–1.4 eV), Ser-37 (–1.4 eV), and Gly-70 (–1.5 eV), which are amino acids physisorbed on the bottom gold surface. Having characterized the PDOS, we are now in a position to calculate the Landauer



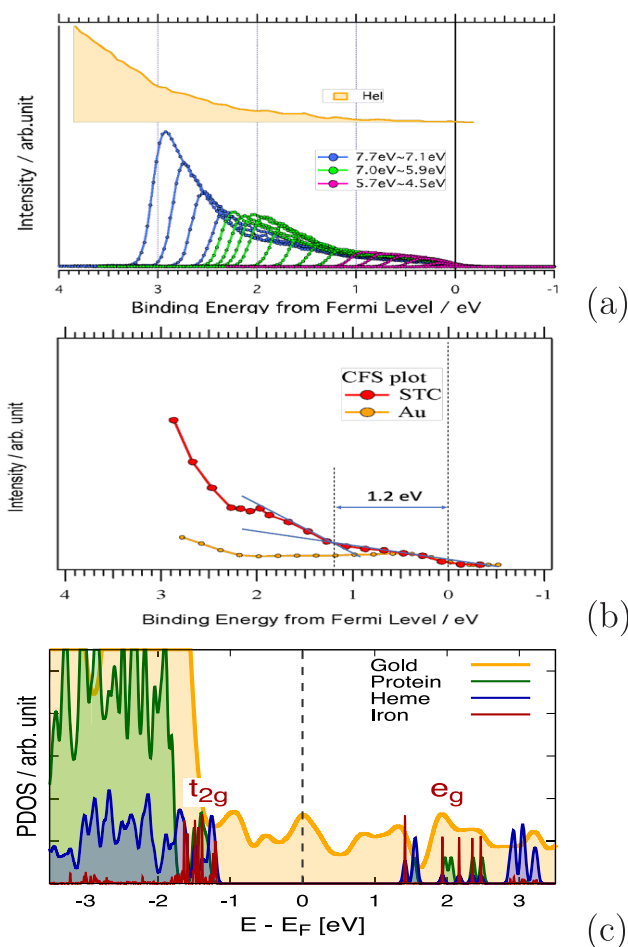


**Figure 3.** (a) Top: UPS signals of STC monolayer on Au substrate with photon excitation energy of HeI (21.2 eV). Bottom: variable, low-energy UV light ( $h\nu$  changes from 4.5 to 7.7 eV, in 0.1 eV steps; every second spectrum is shown, plus all spectra between 7.0 and 6.7 eV). The outer envelope of the 4.5–7.7 eV spectra shows a small peak structure around 2 eV, while the HeI spectrum shows only a monotonic tail (toward 0 eV, the Fermi level). (b) Constant final state yield (CFS) plots at  $E_k = 0.3$  eV for STC on Au and for clean Au films. The latter shows an almost constant feature due to the Au sp band in the 0–2 eV range. In contrast, the CFS plot of STC shows an onset at 1.2 eV due to the photoemission from STC, where the onset energy is determined from the intersection of the two straight lines, drawn on the CFS plot: one for the Au sp levels and one for the protein levels. (c) Projected density of states (PDOS) of STC near the Fermi level  $E_F$ . The states were obtained from Kohn–Sham DFT calculations and localized on protein and gold electrodes by using the projector operator-based diabatization method (POD). The orbital energy of the POD states was shifted by using a computed  $\Sigma$  correction (see the main text and Supporting Information for details).

current and to interpret the measured electronic transport behavior of STC at an atomistic level of detail.

In the Landauer–Büttiker formalism, the tunneling current,  $I$ , is obtained as an integral of the transmission function  $T(E)$  over the Fermi window for a given applied voltage,  $V$ <sup>33</sup>

$$I(V) = \frac{e}{\pi\hbar} \int T(E) [f_L(E, V) - f_R(E, V)] dE \quad (1)$$

where  $E$  is the energy of the tunneling electron and  $f_M$ ,  $M = \{L, R\}$  are the Fermi–Dirac distributions on the left (L) and right (R) electrode, respectively. The calculation of the full (“all-to-all”) transmission function<sup>33</sup>

$$T(E) = \sum_{\alpha, \alpha'} T_{\alpha, \alpha'}(E) = \text{Tr}[\hat{\Gamma}^{(L)}(E) \hat{G}^{(B)\dagger}(E) \hat{\Gamma}^{(R)}(E) \hat{G}^{(B)}(E)] \quad (2)$$

with  $\hat{G}^{(B)}$  being the Green’s function of the bridge (i.e., protein) and  $\hat{\Gamma}^{(M)}$  minus twice the imaginary part of the self-energy, is currently still unfeasible for systems as large as protein junctions. Here, we adopt the commonly used Breit–Wigner (BW) approximation to the full transmission function eq 2,

$$T(E) = \sum_j^{\text{protein}} \frac{\Gamma_j^{(L)}(E) \Gamma_j^{(R)}(E)}{[E - \epsilon_{\Sigma_j}]^2 + \Gamma_j^2(E)}$$

$$\Gamma_j(E) = \frac{1}{2} [\Gamma_j^{(L)}(E) + \Gamma_j^{(R)}(E)] \quad (3)$$

where  $\Gamma_j^{(M)}$  are the diagonal elements of  $\hat{\Gamma}^{(M)}$  in the protein eigenstate basis, i.e., the protein MOs that diagonalize the electronic Hamiltonian of the protein subspace ( $\Gamma_j^{(M)}$  are also termed spectral density functions), and  $\epsilon_{\Sigma_j}$  are the corresponding  $\Sigma$ -corrected energy levels of the protein, as before. The spectral density functions are defined as

$$\Gamma_j^{(M)}(E) = 2\pi \left[ |[\hat{H}_{MP}]_{mj}|^2 \rho_M(\epsilon_{M,m}) \right]_{\epsilon_{M,m}=E} \quad (4)$$

where  $[\hat{H}_{MP}]_{mj}$  are the electronic coupling matrix elements between eigenstate  $j$  of the protein subspace and eigenstate  $m$  of the subspace of electrode  $M$ ,  $\epsilon_{M,m}$  is the energy of state  $m$ , and  $\rho^{(M)}$  is the density of states of electrode  $M$ . The electronic couplings are obtained from POD as the off-diagonal elements between protein and electrode subblocks (see eq S38 in the Supporting Information).

The BW approximation (eq 3) can be formerly derived from the full transmission function eq 2 if one assumes that (i) all off-diagonal elements of the self-energy matrix in the protein eigenstate basis are zero and (ii) the real part of the self-energy is small compared to  $E - \epsilon_{\Sigma_j}$  (see section S4.1 in the Supporting Information for an explicit derivation). Therefore, quantum interference is not accounted for in our calculations, though we expect this effect to be relatively small for the present system. We investigated the accuracy of the BW approximation by considering a simple model of the bridge with  $N$  protein eigenstates coupled to the two electrodes with parameters characteristic for the STC protein (see Supporting Information section S4.2). We find that the transmission function obtained in the BW approximation (eq 3) gives fairly accurate results in this parameter regime when compared to the full transmission matrix (eq 2) (see Figure S6). Hence, we expect the BW approximation to provide a good description for STC.

The results of the current calculations within the BW approximation are summarized in Figure 4. We find that the computed  $I$ – $V$  curve (red line) is in excellent agreement with the experimental data (black line), matching both the shape and the magnitude of the current response. Importantly, the transport is in the off-resonant regime because all occupied protein states are at energies lower than  $-1.2$  eV and outside the Fermi window opened by the experimental voltage range (0.5 V) and so are the unoccupied states. Hence, the current

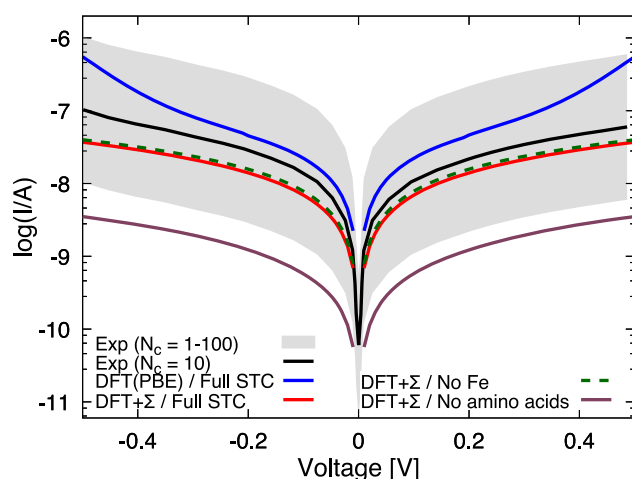


**Figure 4.** Calculated  $I$ – $V$  curves for the Gold-STC-Gold junction shown in Figure 2b. The currents are computed within the Landauer formalism (eq 1) in combination with the independent level or Breit–Wigner approximation (eq 3) using all-QM calculations on the entire junction, specifically projection operator-based diabatization (POD) and DFT(PBE)+ $\Sigma$  (red line). The estimated experimental current per STC protein is shown as black lines. Assuming that the device contains 10 active protein contacts, the current per protein was obtained by dividing the as-measured current shown in Figure 1a by a factor of 10. The likely error bar for this estimate is shown in shaded gray corresponding to 1–100 active protein contacts in the device. The  $I$ – $V$  curve obtained with DFT(PBE), i.e., without  $\Sigma$  correction, is shown in blue.  $I$ – $V$  curves for modified STC structures with Fe atoms replaced by two H atoms (green dashed) and without protein amino acids (purple) are shown for comparison.

increases smoothly with voltage and does not contain any resonant peaks. As the transmission function is flat in the Fermi window, the current response to the applied voltage is practically linear.

We have performed similar calculations for a number of different protein adsorption structures in the “lying” orientation (see Figure 2a) and find that the current is not very sensitive with respect to the particular structure used, at most a factor of 3 difference at 0.5 V; see the following section for a possible explanation. Moreover, the protein is covalently attached to the bottom contact and locked between the electrodes which restricts thermal motion. For these reasons we expect that extensive thermal averaging of the current–voltage response over protein structures—currently computationally intractable—will not change the current–voltage response in a major way. We also performed calculations where the electronic response of the orbitals to the applied voltage was included and found that this had a rather negligible effect on the current (factor of 1.01 at 0.5 V).

To explore how the current–voltage curve would look like in the resonant regime, we shift all protein levels upward by 1.2 eV so that the protein HOMO is aligned with the Fermi levels of the electrode at zero voltage. The shape of the  $I$ – $V$  curve is now rather different (Figure 4, blue line). The resonant molecular states give rise to a rapid increase in the current for small voltages, as one would expect, and there is another stronger increase at about 0.4 V. We assume that in this “artificial gating” experiment the transport still remains coherent, which may not always be the case in practice. For instance, in recent experiments on single molecule junctions it was shown that resonant transport can involve charging/discharging events of the molecule,<sup>46</sup> which are not taken into account in the Landauer formalism used here. These nonlinear responses, induced by the shifted valence band peaks of the protein within the Fermi window, are not seen in experiment and a further confirmation that electron transport is indeed in the off-resonant tunneling regime.

Which protein states mediate the tunneling current? To answer this question, we plot in Figure 5a the contribution of each protein state to the total current at a voltage of 0.5 V

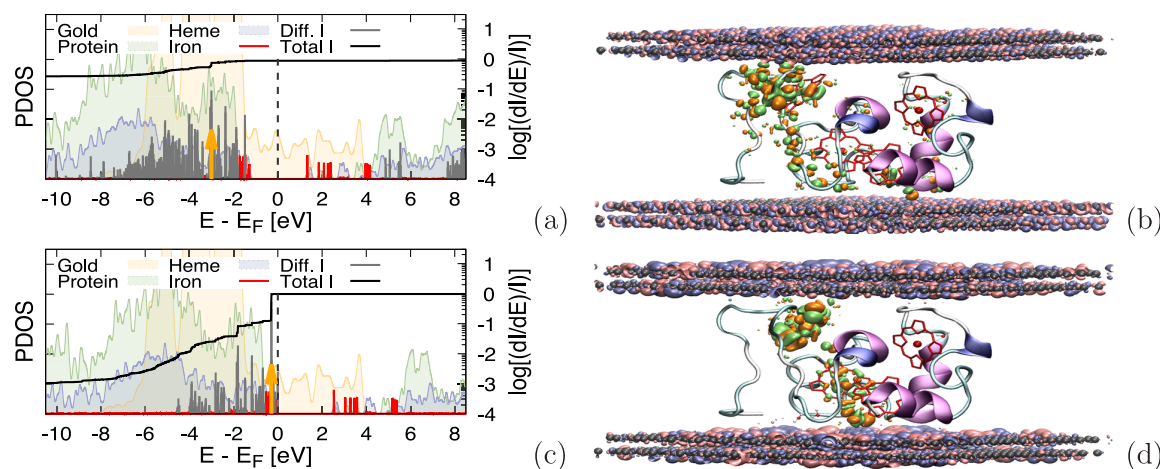


**Figure 5.** Breakdown of the total current in contributions from molecular orbitals of the STC protein. In (a) the differential current contributions  $\log[(dI/dE)/I]$  (gray bars) to the total current  $\int_{-\infty}^E (dI/dE')/I dE'$  (black line) are shown for all molecular orbitals. The orbitals are the same as the ones used for the current calculation in Figure 4 (i.e., obtained from POD calculation in combination with DFT(PBE)+ $\Sigma$ ) and are shown relative to the Fermi level of the electrodes at zero voltage. The corresponding projected density of states (PDOS) is shown as well and broken down in contributions from gold, protein amino acids, heme, and iron. In (b) the molecular orbital with the highest contribution to the current (marked by an orange arrow in (a)) is depicted in orange and green isosurfaces. The two metallic states in the bottom and top electrodes having the same energy as the molecular orbital shown are depicted in blue and pink isosurfaces. The analogous data for the (hypothetical) resonant tunneling regime where the molecular orbitals are shifted upward by 1.2 eV are shown in (c) and (d).

(gray bars) as well as the accumulated sum (black line). The corresponding projected density of states is shown as well. We find that the current is the result of many small contributions originating from protein and heme states at energies between about  $-8$  and  $-2$  eV. These states are typically delocalized over two or three heme cofactors that bridge the two electrodes (20–25%) and the protein amino acids (80–75%). As a representative example, we show the molecular orbital of STC with the largest contribution to the total current, 8.8% (positioned at  $-3.0$  eV), in Figure 5b. Interestingly, the highest valence band states of the protein composed of the Fe  $d_{t_{2g}}$ -heme orbitals contribute very little to the current, even though these states are closest in energy to the Fermi window. The reason is that their coupling to the electrode ( $\Gamma^{(L)}$  and  $\Gamma^{(R)}$ ) is much smaller than for the most conductive states since they are mostly localized on the heme and do not spread over the amino acids that are in van der Waals contact with the electrodes. Unoccupied states up to 10 eV above the Fermi level were involved in the calculations; however, their contribution to the tunneling current is negligible (see Figure 5a). In particular, Fe  $e_g$ -heme orbitals located at the conduction band edge do not affect the currents, and the conductivity is mediated predominantly by the valence-band states.

The result obtained from DFT+ $\Sigma$  calculations—a large number of protein conduction channels, each contributing a small fraction to the total current—is not inconsistent with the single-channel Landauer model that we used to fit the experimental data. It just means that for the purpose of fitting the current the large number of protein conduction channels obtained from DFT+ $\Sigma$  calculations can be replaced to a good approximation by a single effective conduction channel. Moreover, we note that the large number of protein conduction channels renders the current less sensitive to protein thermal fluctuations, which may explain why the calculated current is rather insensitive with respect to the specific adsorption structure in the lying orientation.

The situation is strikingly different for the (hypothetical) resonant regime considered before where all protein states are shifted upward by 1.2 eV. The current contributions and projected density of states are shown in Figure 5c. In this regime, 83% of the current is due to the highest valence band states composed of Fe  $d_{t_{2g}}$ -heme orbitals, typically delocalized over 2–3 hemes, and the contribution of states delocalized over the amino acids is significantly reduced. The reason is that the constant shift increases the area under the transmission peak in the Fermi window much more strongly for the Fe  $d_{t_{2g}}$  valence band states (which become near-resonant after the shift) than for the states delocalized over the amino acids (which still remain off-resonant after the shift). The conduction channel with the highest contribution (Figure 5d) is delocalized mostly on the first and second hemes (H1 and H2 in Figure 2b) and partly on H3, hence forming an ideal connection between the two electrodes. This results in strong and relatively symmetric coupling values compared to most other conduction channels ( $\Gamma^{(L)} = 13.4$  meV and  $\Gamma^{(R)} = 2.0$  meV) and gives rise to a relatively broad transmission peak of significant height ( $T = 0.45$ ).

To further understand the role of Fe, heme cofactors, and protein amino acids in determining conductance of STC, we calculated the current–voltage curve for two different protein modifications, all based on the same Gold-STC-Gold structural model used before: (i) the Fe atom in each heme is replaced

by two H atoms; (ii) all protein amino acids are removed, retaining only the Fe-heme cofactors, axial histidines, and cysteine linkages. We find that replacement of Fe has virtually no effect on the current–voltage response (see red vs dashed green line in Figure 4). By contrast, removal of all protein amino acids leads to a significant drop in the tunneling current by 1 order of magnitude (purple line). Considering the analysis of the conduction channels in the unmodified STC protein, this result is not unexpected. It shows that in the present off-resonant regime most of the coupling with the electrodes is due to protein amino acids and that the mixing of the protein states with the Fe-heme states is not essential. The insignificant role of Fe for conduction is in line with previous experimental measurements of conductance in Fe-containing and Fe-free cytochrome *c*.<sup>47</sup>

Combining temperature-dependent conductance measurements, photoemission spectroscopy (UPS), and large-scale DFT+ $\Sigma$  calculations, we have uncovered the conduction mechanism through solid state multi-heme protein junctions. The data unequivocally rule out activated hopping and strongly suggest off-resonant coherent tunneling over  $\sim 3$  nm as the dominating conduction mechanism. DFT+ $\Sigma$  calculations within the Landauer formalism show that the active transport channels (i.e., MOs of STC) are delocalized over typically 2–3 hemes and strongly mix with orbitals of amino acid residues that are in van der Waals contact with the electrodes. We find that the total current is a collective effect of a few hundred of such states, each contributing a small fraction. The reason for this is that the valence band edge of STC is rather deep in energy in the monolayer junctions ( $\leq -1.2$  eV with respect to the Fermi energy of the electrodes), giving rise to a flat transmission function in the Fermi window for each conduction channel. The same picture may explain previous single molecule STM measurements for the deca-heme proteins MtrC<sup>25</sup> and MtrF.<sup>24</sup> However, the partial protein solvation and the possibly different energy level alignment in those measurements might tip the balance between this and other mechanisms. While general and in principle applicable to any protein junction, our computational approach is currently limited to proteins of no more than about 100–150 residues. Hence,  $I$ – $V$  calculations on MtrC or MtrF similar to the ones presented here for STC are currently still out of reach.

Our findings imply that the mechanism for electronic conduction through solid MHCs monolayers in a vacuum is fundamentally different from chemically<sup>18</sup> or photochemically<sup>11</sup> induced electron transfer across the same protein in aqueous solution. While the latter proceeds via consecutive Fe<sup>2+/3+</sup> hopping mediated by the redox-active Fe  $d(t_{2g})$ -heme orbitals at the top of the valence band, conduction occurs by a manifold of valence band states delocalized over heme and protein amino acids. The role of the protein matrix is to augment the tails of the heme orbitals to increase the electronic coupling with the electrodes: without such contributions to the coupling, the protein conduction sharply decreases because the heme edges cannot fully approach the electrodes due to steric hindrance. Our results thus provide now an explanation for the earlier experimental finding that conduction through cytochrome *c* does not require Fe,<sup>47</sup> whereas iron is mandatory for electron transfer redox activity. Still, in STC Fe has an important structural role keeping the protein rigid and preventing unfolding of the main secondary structure motifs when the protein adsorbs on the metal surface, according to our MD simulations.



Intriguingly, the conduction mechanism changes qualitatively in the resonant regime where the protein valence-band edge is aligned with the Fermi energy as reported recently for cytochrome *c*<sup>48</sup> and earlier for azurin.<sup>49</sup> In this scenario, the electron transport is dominated by the familiar Fe d(*t*<sub>2g</sub>)-heme orbitals that mediate electron hopping in solution, more specifically by linear combinations thereof with contributions of 2–3 hemes that bridge the space between the electrodes. Hence, by tuning the energy offset between the protein states and the electrode work function, which can in principle be done by suitable protein mutations, surface modifications or application of a gating potential, as reported recently for azurin,<sup>50</sup> one can control the active states for electron transport. Although such modifications might be, and certainly the solid state gating still is, nontrivial in practice, knowledge of the electronic states and their positions provides useful guidance for control and design of bioelectronic devices.

## ■ ASSOCIATED CONTENT

### Supporting Information

The Supporting Information is available free of charge at <https://pubs.acs.org/doi/10.1021/acs.jpclett.0c02686>.

A full description of the fitting of the experimental *I*–*V* curves, generation of an atomistic structure of the Au-STC-Au junction, UPS band alignment measurements, DFT+ $\Sigma$  calculations on the junctions, dominant conduction channels in off-resonant as well as resonant regime (PDF)

## ■ AUTHOR INFORMATION

### Corresponding Author

Jochen Blumberger – Department of Physics and Astronomy, University College London, London WC1E 6BT, U.K.; [orcid.org/0000-0002-1546-6765](https://orcid.org/0000-0002-1546-6765); Phone: ++44-(0)20-7679-4373; Email: [j.blumberger@ucl.ac.uk](mailto:j.blumberger@ucl.ac.uk); Fax: ++44-(0)20-7679-7145

### Authors

Zdenek Futera – Faculty of Science, University of South Bohemia, 370 05 Ceske Budejovice, Czech Republic; Department of Physics and Astronomy, University College London, London WC1E 6BT, U.K.; [orcid.org/0000-0003-0471-8194](https://orcid.org/0000-0003-0471-8194)

Ichiro Ide – Graduate School of Science and Engineering, Chiba University, Chiba, Japan

Ben Kayser – Department of Materials and Interfaces, Weizmann Institute of Science, Rehovot, Israel; [orcid.org/0000-0002-1482-1825](https://orcid.org/0000-0002-1482-1825)

Kavita Garg – Department of Materials and Interfaces, Weizmann Institute of Science, Rehovot, Israel

Xiuyun Jiang – Department of Physics and Astronomy, University College London, London WC1E 6BT, U.K.; [orcid.org/0000-0001-6884-411X](https://orcid.org/0000-0001-6884-411X)

Jessica H. van Wonderen – School of Chemistry, School of Biological Sciences, University of East Anglia, Norwich NR4 7TJ, U.K.; [orcid.org/0000-0003-0764-5453](https://orcid.org/0000-0003-0764-5453)

Julea N. Butt – School of Chemistry, School of Biological Sciences, University of East Anglia, Norwich NR4 7TJ, U.K.; [orcid.org/0000-0002-9624-5226](https://orcid.org/0000-0002-9624-5226)

Hisao Ishii – Graduate School of Science and Engineering, Chiba University, Chiba, Japan

Israel Pecht – Department of Immunology, Weizmann Institute of Science, Rehovot, Israel

Mordechai Sheves – Department of Organic Chemistry, Weizmann Institute of Science, Rehovot, Israel; [orcid.org/0000-0002-5048-8169](https://orcid.org/0000-0002-5048-8169)

David Cahen – Department of Materials and Interfaces, Weizmann Institute of Science, Rehovot, Israel; [orcid.org/0000-0001-8118-5446](https://orcid.org/0000-0001-8118-5446)

Complete contact information is available at: <https://pubs.acs.org/doi/10.1021/acs.jpclett.0c02686>

### Notes

The authors declare no competing financial interest.

## ■ ACKNOWLEDGMENTS

Z.F. was supported by EPSRC (EP/M001946/1) and by the European Research Council (ERC) under the European Union's Horizon 2020 research and innovation programme (grant agreement no. 682539/SOFTCHARGE). X.J. was supported by a Ph.D. studentship cosponsored by the Chinese Scholarship Council and University College London. J.H.v.W. was supported by EPSRC (EP/M001989/1). I.I. and H.I. were supported by JSPS KAKENHI Grant 16H04222. M.S. and D.C. thank the Israel Science Foundation and the German Science Foundation (DFG) for partial support. Via UCL-group membership of the UK's HEC Materials Chemistry Consortium, which is funded by EPSRC (EP/L000202, EP/R029431), this work used the ARCHER UK National Supercomputing Service (<http://www.archer.ac.uk>). We are grateful to the UK Materials and Molecular Modelling Hub for computational resources, which is partially funded by EPSRC (EP/P020194/1).

## ■ REFERENCES

- (1) Jiang, X.; van Wonderen, J. H.; Butt, J. N.; Edwards, M. J.; Clarke, T. A.; Blumberger, J. Which Multi-Heme Protein Complex Transfers Electrons More Efficiently? Comparing MtrCAB from *Shewanella* with OmcS from *Geobacter*. *J. Phys. Chem. Lett.* **2020**, 9421.
- (2) Chong, G. W.; Karbelkar, A. A.; El-Naggar, M. Y. Nature's Conductors: What Can Microbial Multi-Heme Cytochromes Teach Us About Electron Transport and Biological Energy Conversion? *Curr. Opin. Chem. Biol.* **2018**, 47, 7–17.
- (3) Blumberger, J. Electron Transfer and Transport through Multi-Heme Proteins: Recent Progress and Future Directions. *Curr. Opin. Chem. Biol.* **2018**, 47, 24–31.
- (4) Paixao, V. B.; Salgueiro, C. A.; Brennan, L.; Reid, G. A.; Chapman, S. K.; Turner, D. L. The Solution Structure of a Tetraheme Cytochrome from *Shewanella frigidimarina* Reveals a Novel Family Structural Motif. *Biochemistry* **2008**, 47, 11973–11980.
- (5) Clarke, T. A.; Edwards, M. J.; Gates, A. J.; Hall, A.; White, G. F.; Bradley, J.; Reardon, C. L.; Shi, L.; Beliaev, A. S.; Marshall, M. J.; et al. Structure of a Bacterial Cell Surface Decaheme Electron Conduit. *Proc. Natl. Acad. Sci. U. S. A.* **2011**, 108, 9384–9389.
- (6) Edwards, M. J.; Hall, A.; Shi, L.; Fredrickson, J.; Zachara, J. M.; Butt, J. N.; Richardson, D. J.; Clarke, T. A. The Crystal Structure of the Extracellular 11-Heme Cytochrome UndA Reveals a Conserved 10-Heme Motif and Defined Binding Site for Soluble Iron Chelates. *Structure* **2012**, 20, 1275–1284.
- (7) Edwards, M. J.; White, G. F.; Norman, M.; Tome-Fernandez, A.; Ainsworth, E.; Shi, L.; Fredrickson, J. K.; Zachara, J. M.; Butt, J. N.; Richardson, D. J.; Clarke, T. A. Extracellular Decaheme Proteins Involved in Microbe-Mineral Electron Transfer. *Sci. Rep.* **2015**, 5, 11677.

- (8) Edwards, M. J.; White, G. F.; Butt, J. N.; Richardson, D. J.; Clarke, T. A. The Crystal Structure of a Biological Insulated Transmembrane Molecular Wire. *Cell* **2020**, *181*, 1–9.
- (9) Wang, F.; Gu, Y.; O'Brien, J. P.; Yi, M. S.; Yalcin, S. E.; Srikanth, V.; Shen, C.; Vu, D.; Ing, N. L.; Hochbaum, A. I.; et al. Structure of Microbial Nanowires Reveals Stacked Hemes that Transport Electrons over Micrometers. *Cell* **2019**, *177*, 361–369.
- (10) Filman, D. J.; Marino, S. F.; Ward, J. E.; Yang, L.; Mester, Z.; Bullitt, E.; Lovley, D. R.; Strauss, M. Cryo-EM Reveals the Structural Basis of Long-Range Electron Transport in a Cytochrome-based Bacterial Nanowire. *Commun. Biol.* **2019**, *2*, 219.
- (11) van Wonderen, J. H.; Hall, C. R.; Jiang, X.; Adamczyk, K.; Carof, A.; Heisler, I.; Piper, S. E. H.; Clarke, T. A.; Watmough, N. J.; Sazanovich, I. V.; et al. Ultrafast Light-Driven Electron Transfer in a Ru(II)tris(bipyridine)-Labeled Multiheme Cytochrome. *J. Am. Chem. Soc.* **2019**, *141*, 15190–15200.
- (12) van Wonderen, J. H.; Li, D.; Piper, S. E. H.; Lau, C. Y.; Jenner, L. P.; Hall, C. R.; Clarke, T. A.; Watmough, N. J.; Butt, J. N. Photosensitized Multiheme Cytochromes as Light-Driven Molecular Wires and Resistors. *ChemBioChem* **2018**, *19*, 2206–2215.
- (13) Polizzi, N. F.; Skourtis, S. S.; Beratan, D. N. Physical Constraints on Charge Transport through Bacterial Nanowires. *Faraday Discuss.* **2012**, *155*, 43–62.
- (14) Jiang, X.; Burger, B.; Gajdos, F.; Bortolotti, C.; Futera, Z.; Breuer, M.; Blumberger, J. Kinetics of Trifurcated Electron Flow in the Decaheme Bacterial Proteins MtrC and MtrF. *Proc. Natl. Acad. Sci. U. S. A.* **2019**, *116*, 3425–3430.
- (15) Jiang, X.; Futera, Z.; Ali, M. E.; Gajdos, F.; von Rudorff, G. F.; Carof, A.; Breuer, M.; Blumberger, J. Cysteine Linkages Accelerate Electron Flow through Tetra-Heme Protein STC. *J. Am. Chem. Soc.* **2017**, *139*, 17237–17240.
- (16) Breuer, M.; Rosso, K. M.; Blumberger, J. Electron Flow in Multiheme Bacterial Cytochromes is a Balancing Act Between Heme Electrostatic Interaction and Redox Potentials. *Proc. Natl. Acad. Sci. U. S. A.* **2014**, *111*, 611–616.
- (17) Breuer, M.; Zarzycki, P.; Shi, L.; Clarke, T. A.; Edwards, M. J.; Butt, J. N.; Richardson, D. J.; Fredrickson, J. K.; Zachara, J. M.; Blumberger, J.; Rosso, K. M. Molecular Structure and Free Energy Landscape for Electron Transport in the Decaheme Cytochrome MtrF. *Biochem. Soc. Trans.* **2012**, *40*, 1198–1203.
- (18) Blumberger, J. Recent Advances in the Theory and Molecular Simulation of Biological Electron Transfer Reactions. *Chem. Rev.* **2015**, *115*, 11191–11238.
- (19) Szczesny, J.; Markovic, N.; Conzuelo, F.; Zacarias, S.; Pereira, I. A. C.; Lubitz, W.; Plumere, N.; Schuhmann, W.; Ruff, A. A Gas Breathing Hydrogen/Air Biofuel Cell Comprising a Redox Polymer/Hydrogenase-Based Bionanode. *Nat. Commun.* **2018**, *9*, 4715.
- (20) Bostick, C. D.; Mukhopadhyay, S.; Pecht, I.; Sheves, M.; Cahen, D.; Lederman, D. Protein Bioelectronics: A Review of What We Do and Do Not Know. *Rep. Prog. Phys.* **2018**, *81*, 026601.
- (21) Wu, J.; Lan, Z.; Lin, J.; Huang, M.; Hao, S.; Sato, T.; Yin, S. A Novel Thermosetting Gel Electrolyte for Stable Quasi-Solid-State Dye-Sensitized Solar Cells. *Adv. Mater.* **2007**, *19*, 4006–4011.
- (22) Garg, K.; Ghosh, M.; Eliash, T.; van Wonderen, J. H.; Butt, J. N.; Shi, L.; Jiang, X.; Zdenek, F.; Blumberger, J.; Pecht, I.; Sheves, M.; Cahen, D. Direct Evidence for Heme-Assisted Solid-State Electronic Conduction in Multi-Heme c-Type Cytochromes. *Chem. Sci.* **2018**, *9*, 7304–7310.
- (23) Sepunaru, L.; Pecht, I.; Sheves, M.; Cahen, D. Solid-State Electron Transport across Azurin: From a Temperature-Independent to a Temperature-Activated Mechanism. *J. Am. Chem. Soc.* **2011**, *133*, 2421–2423.
- (24) Byun, H. S.; Pirbadian, S.; Nakano, A.; Shi, L.; El-Naggar, M. Y. Kinetic Monte Carlo Simulations and Molecular Conductance Measurements of the Bacterial Decaheme Cytochrome MtrF. *ChemElectroChem* **2014**, *1*, 1932–1939.
- (25) Wigginton, N. S.; Rosso, K. M.; Lower, B. H.; Shi, L.; Hochella, M. F. J. Electron Tunneling Properties of Outer-Membrane Decaheme Cytochromes from *Shewanella oneidensis*. *Geochim. Cosmochim. Acta* **2007**, *71*, 543–555.
- (26) Wigginton, N. S.; Rosso, K. M.; Hochella, M. F. J. Mechanism of Electron Transfer in Two Decaheme Cytochromes from a Metal-Reducing Bacterium. *J. Phys. Chem. B* **2007**, *111*, 12857–12864.
- (27) Pirbadian, S.; El-Naggar, M. Y. Multistep Hopping and Extracellular Charge Transfer in Microbial Redox Chains. *Phys. Chem. Chem. Phys.* **2012**, *14*, 13802–13808.
- (28) Futera, Z.; Blumberger, J. Electronic Couplings for Charge Transfer across Molecule/Metal and Molecule/Semiconductor Interfaces: Performance of the Projector Operator-Based Diabatization Approach. *J. Phys. Chem. C* **2017**, *121*, 19677–19689.
- (29) Marcus, R. A.; Sutin, N. Electron Transfer in Chemistry and Biology. *Biochim. Biophys. Acta, Rev. Bioenerg.* **1985**, *811*, 265–322.
- (30) Chidsey, C. E. D. Free Energy and Temperature Dependence of Electron Transfer at the Metal-electrolyte Interface. *Science* **1991**, *251*, 919–922.
- (31) Simmons, J. G. Generalized Formula for the Electric Tunnel Effect between Similar Electrodes Separated by a Thin Insulating Film. *J. Appl. Phys.* **1963**, *34*, 1793–1803.
- (32) Carey, R.; Chen, L.; Gu, B.; Franco, I. When Can Time-Dependent Currents Be Reproduced by the Landauer Steady-State Approximation? *J. Chem. Phys.* **2017**, *146*, 174101.
- (33) Nitzan, A. *Chemical Dynamics in Condensed Phases: Relaxation, Transfer, and Reactions in Condensed Molecular Systems*; Oxford University Press, 2006.
- (34) Valianti, S.; Cuevas, J.-C.; Skourtis, S. S. Charge-Transport Mechanism in Azurin-Based Monolayer Junctions. *J. Phys. Chem. C* **2019**, *123*, 5907.
- (35) Iori, F.; Di Felice, R.; Molinari, E.; Corni, S. GoIP: An Atomistic Force-Field to Describe the Interaction of Proteins With Au(111) Surfaces in Water. *J. Comput. Chem.* **2009**, *30*, 1465–1476.
- (36) Wright, L. B.; Rodger, P. M.; Corni, S.; Walsh, T. R. GoIP-CHARMM: First-Principles Based Force Fields for the Interaction of Proteins with Au(111) and Au(100). *J. Chem. Theory Comput.* **2013**, *9*, 1616–1630.
- (37) Futera, Z.; Blumberger, J. Adsorption of Amino Acids on Gold: Assessing the Accuracy of the GoIP-CHARMM Force Field and Parametrization of Au-S Bonds. *J. Chem. Theory Comput.* **2019**, *15*, 613–624.
- (38) Ollila, O. H. S.; Risselada, H. J.; Louhivuori, M.; Lindahl, E.; Vattulainen, I.; Marrink, S. J. 3D Pressure Field in Lipid Membranes and Membrane-Protein Complexes. *Phys. Rev. Lett.* **2009**, *102*, 78101.
- (39) Hutter, J.; Iannuzzi, M.; Schiffmann, F.; VandeVondele, J. CP2K: Atomistic Simulations of Condensed Matter Systems. *WIREs Comput. Mol. Sci.* **2014**, *4*, 15–25.
- (40) Goedecker, S.; Teter, M.; Hutter, J. Separable Dual-Space Gaussian Pseudopotential. *Phys. Rev. B: Condens. Matter Mater. Phys.* **1996**, *54*, 1703–1710.
- (41) Perdew, J. P.; Burke, K.; Ernzerhof, M. Generalized Gradient Approximation Made Simple. *Phys. Rev. Lett.* **1996**, *77*, 3865–3868.
- (42) Neaton, J. B.; Hybertsen, M. S.; Louie, S. G. Renormalization of Molecular Electronic Levels at Metal-Molecule Interfaces. *Phys. Rev. Lett.* **2006**, *97*, 216405.
- (43) Darancet, P.; Widawsky, J. R.; Choi, H. J.; Venkataraman, L.; Neaton, J. B. Quantitative Current-Voltage Characteristics in Molecular Junctions from First Principles. *Nano Lett.* **2012**, *12*, 6250–6254.
- (44) Egger, D. A.; Liu, Z.-F.; Neaton, J. B.; Kronik, L. Reliable Energy Level Alignment at Physisorbed Molecule-Metal Interfaces from Density Functional Theory. *Nano Lett.* **2015**, *15*, 2448–2455.
- (45) Liu, Z.-F.; Egger, D. A.; Refaely-Abramson, S.; Kronik, L.; Neaton, J. B. Energy Level Alignment at Molecule-Metal Interfaces from an Optimally Tuned Range Separated Hybrid Functional. *J. Chem. Phys.* **2017**, *146*, 092326.
- (46) Fung, E.-D.; Gelbwaser, D.; Taylor, J.; Low, J.; Xia, J.; Davydenko, I.; Campos, L. M.; Marder, S.; Peskin, U.; Venkataraman, L. Breaking Down Resonance: Nonlinear Transport and the



Breakdown of Coherent Tunneling Models in Single Molecule Junctions. *Nano Lett.* **2019**, *19*, 2555–2561.

(47) Amdursky, N.; Ferber, D.; Pecht, I.; Sheves, M.; Cahen, D. Redox Activity Distinguishes Solid-State Electron Transport from Solution-Based Electron Transfer in a Natural and Artificial Protein: Cytochrome C and Hemin-Doped Human Serum Albumin. *Phys. Chem. Chem. Phys.* **2013**, *15*, 17142–17149.

(48) Fereiro, J. A.; Kayser, B.; Romero-Muniz, C.; Vilan, A.; Dolgikh, D. A.; Chertkova, R. V.; Cuevas, J. C.; Zotti, L. A.; Pecht, I.; Sheves, M.; et al. A Solid-State Protein Junction Serves as a Bias-Induced Current Switch. *Angew. Chem., Int. Ed.* **2019**, *58*, 11852–11859.

(49) Fereiro, J. A.; Yu, X.; Pecht, I.; Sheves, M.; Cuevas, J. C.; Cahen, D. Tunneling Explains Efficient Electron Transport via Protein Junctions. *Proc. Natl. Acad. Sci. U. S. A.* **2018**, *115*, 4577–4583.

(50) Kayser, B.; Fereiro, J. A.; Guo, C.; Cohen, S. R.; Sheves, M.; Pecht, I.; Cahen, D. Transistor Configuration Yields Energy Level Control in Protein-Based Junctions. *Nanoscale* **2018**, *10*, 21712–21720.